applied sciences

MDPI

Article

Interference Spectral Imaging Based on Liquid Crystal Relaxation and Its Application in Optical Component Defect Detection

Jiajia Yuan [1,2], Wei Fan [1,2,*], He Cheng [1], Dajie Huang [1] and Tongyao Du [1,3]

[1] National Laboratory on High Power Laser and Physics, Shanghai Institute of Optics and Fine Mechanics, Chinese Academy of Sciences, Shanghai 201800, China; yuanjiajia@siom.ac.cn (J.Y.); chenghe@siom.ac.cn (H.C.); hdajie@siom.ac.cn (D.H.); tydu@siom.ac.cn (T.D.)
[2] Center of Materials Science and Optoelectronics Engineering, University of Chinese Academy of Sciences, Beijing 100049, China
[3] Department of Optics and Optical Engineering, University of Science and Technology of China, Hefei 230026, China
* Correspondence: fanweil@siom.ac.cn; Tel.: +86-137-9541-6889

Abstract: In this paper, we propose a fast interference spectral imaging system based on liquid crystal (LC) relaxation. The path delay of nematic LC during falling relaxation is used for the scanning of the optical path. Hyperspectral data can be obtained by Fourier transforming the data according to the path delay. The system can obtain two-dimensional spatial images of arbitrary wavelengths in the range of 300–1100 nm with a spectral resolution of 262 cm^{-1}. Compared with conventional Fourier transform spectroscopy, the system can easily collect and integrate all valid information within 20 s. Based on the LC, controlling the optical path difference between two orthogonally polarized beams can avoid mechanical movement. Finally, the potential for application in contactless and rapid non-destructive optical component defect inspection is demonstrated.

Keywords: interference spectral imaging; LC delayer; LC relaxation; optics inspection

check for updates

Citation: Yuan, J.; Fan, W.; Cheng, H.; Huang, D.; Du, T. Interference Spectral Imaging Based on Liquid Crystal Relaxation and Its Application in Optical Component Defect Detection. *Appl. Sci.* **2022**, *12*, 718. https://doi.org/10.3390/app12020718

Academic Editor: Dick Sterenborg

Received: 14 December 2021
Accepted: 8 January 2022
Published: 12 January 2022

Publisher's Note: MDPI stays neutral with regard to jurisdictional claims in published maps and institutional affiliations.

Copyright: © 2022 by the authors. Licensee MDPI, Basel, Switzerland. This article is an open access article distributed under the terms and conditions of the Creative Commons Attribution (CC BY) license (https://creativecommons.org/licenses/by/4.0/).

1. Introduction

Precision optical components have a wide range of applications in many fields. The quality of optical elements directly affects the performance of the whole optical system. Therefore, optical element damage detection has attracted increasing attention. Machine vision provides a reliable real-time detection method [1]. Nonlinear optical imaging can detect important properties such as crystal orientation and boundaries [2]. Laser speckle technology can detect micro vibrating objects [3]. LCs have excellent optical properties and have been used in LC wave plates [4], LC tunable filters [5], LC polarization gratings [6], and variable delay devices [7]. LC has also been proposed for use in optical fiber sensing [8], lasers [9], spectral imaging [10], and other fields. Among these, LC spectral imaging technology achieves spectral imaging with high spatial and spectral resolutions. Owing to their small size, light weight, low power consumption, flexibility, and convenience of use, LCs have attracted attention for research on spectral imaging. We consider whether spectral imaging based on LC can be used in optical component defect detection.

The most-used LC spectral imaging technique is based on a liquid crystal tunable filter (LCTF) that can perform continuous spectral tuning by altering the center wavelength of the filter. The Japan Aerospace Exploration Agency (JAXA) was the first organization to research LC spectral imaging [11]. In order to obtain a narrower bandwidth, cascaded LC was used based on a LCTF [12]. Combining the two structures of a Solc filter and a Lyot filter can achieve high efficiency and a narrower full width at half maximum [13]. However, the LCTF requires multiple LC cells to work simultaneously, which leads to defects in the uniformity of the light-passing surface and acquisition time. In addition, the LCTF has

been investigated for compressive sensing, which can improve the spectral and spatial resolutions [14]. However, the complex and time-consuming acquisition and calculations were found to be drawbacks. Additionally, the LCTFs used in spectral imaging systems are complicated and use multiple LCs devices with significant costs.

The combination of LC and interference spectral imaging technology is another important LC spectral imaging technique. This technique can obtain spectral information on the measured object using the Fourier transform of the interferogram. In double-beam interference, the interferogram is obtained by varying the optical path difference between the coherent beams. Therefore, the birefringence effect of the LCs introduces an optical path difference between the two coherent beams. Interferometric spectral imaging using LC delayers was proposed in 1990 [15]. However, in recent years, owing to the development of high-speed charge-coupled devices (CCDs) [16], and data recording and processing capabilities, LC delayers have become a key component in spectral imaging.

By varying the driving voltage of the LC, a series of interferogram images can be recorded. Spectral reconstruction can be realized using the interference spectral imaging theory [17]. However, a short acquisition time and a high spectral resolution cannot be achieved simultaneously. In order to improve the spectral resolution by using multiple reflections to increase the optical path difference, Huang obtained a resolution of 1 nm @ 630 nm [18]. However, this technique cannot be used to obtain two-dimensional spatial data.

In addition, Jullien et al. proposed dynamically driving a 195-µm-thick LC with a step voltage, constituting an optical delay line, in combination with a periodic interferometric spectrum to obtain the relationship between the relative delay and the optical path between the two waves [19]. Furthermore, they applied imaging to tilted cholesteric LC structures [20]. A spectral resolution of 130 cm^{-1} (6 nm) was achieved at 400–1000 nm in 130 s by using a thicker LC with a fourfold improvement in the spectral resolution [17]. Using a thick wedge-shaped LC through a space along the passive path, hyperspectral images were obtained [21]. The large amount of processing resources required means that it is time consuming to acquire hyperspectral images.

Based on previous studies, this paper describes a compact, non-mechanical, high-resolution fast Fourier transform spectroscopy system based on LC delayers. The relaxation characteristics of LC are utilized to quickly obtain the interference intensity corresponding to different optical paths. By measuring the continuous change in light intensity during the LC relaxation time, optical paths with different times can be obtained quickly. The hyperspectral imaging speed can be improved using LC delayers. The application of this system in optical component defect detection is also demonstrated.

2. Theory of Interferometric Spectral Imaging Based on Liquid Crystal Delayers

Interferometric imaging spectroscopy is an imaging technology that simultaneously obtains spatial and spectral information on the measured object through an interferometric imaging system. It uses the Fourier transform relationship between the interferogram and the restored spectrum and obtains the spectral information on the measured object using the Fourier integral transform of the interferogram.

Based on the basic principles of interference spectrum imaging [22], Equation (1) shows that $I(\Delta)$ and $B(\sigma)$ are a pair of Fourier transform pairs, $B(\sigma)$ is the spectrum of the polychromatic light, $I(\Delta)$ is the two-beam interference intensity distribution, Δ is the optical path difference delay between the two beams, and σ is the wavenumber.

$$B(\sigma) = \int_{-\infty}^{\infty} I(\Delta) \cos(2\pi\sigma\Delta) d\Delta \quad (1)$$

This principle can be used for spectral imaging to obtain the intensity distribution for different wavelengths. The acquisition of the interferometric intensity with different optical path differences is the most important part of interference spectral imaging.

A LC cell is made of a nematic LC mixture (HTD028200-200) that is inserted between two quartz glass substrates coated with an indium tin oxide (ITO) conductive film. Polyimide (PI) is deposited over the ITO and rubbed to make the LC molecules essentially parallel to the substrates. The LC cell we used has a small pretilt angle (6°).

An external electric or magnetic field can change the alignment of the LC molecules. According to the electro-optical Fredericks effect [23], the LC does not deform when the driving voltage is less than the threshold voltage. When the applied voltage is higher than the threshold voltage, the LC undergoes deformation to minimize the free energy. The Fredericks transformation studied in this paper was carried out under strong anchoring conditions. When a LC material with positive dielectric anisotropy (positive LC) is used, the LC molecules will change from the arrangement along the surface to the vertical plane under the action of an electric field along the normal direction of the LC surface. This effect changes the refractive index of the extraordinary axis of the LC, while the ordinary axis remains constant. This means that $\Delta n = n_e - n_0$ changes with the driving voltage, where n_0 and n_e are the ordinary and extraordinary refractive indices, respectively. However, the change in the direction of the LC molecules due to the minimum free energy takes some time, defined as the relaxation time of the LC molecules. For a thin LC, the relaxation time of the LC is approximately 10–200 ms [24,25] (p. 244) (p. 184).

The rising relaxation time of a LC is the time required for the LC molecules to reach a new equilibrium position from their initial alignment orientation under a loading external field. Correspondingly, the falling relaxation time is the time required for the LC molecules to return from their orientation position in the high-energy state to the initial stable state when the driving field is removed, owing to its elasticity. In LC interferometric spectroscopy imaging, the birefringence effect of the LC can be used to obtain the interference intensity at different delay times by adjusting the voltage. However, this method is time-consuming. Using the relaxation characteristics of the LC, different optical path differences can be obtained for different refractive index differences in the LC during the loading or unloading of the driving voltage.

The response times for decay (τ_d) and rise (τ_r) can be described by the following equation [26]:

$$\tau_d = \frac{\gamma_1 L^2}{4K_{33}\left(\frac{\pi}{2} - \frac{\theta_p}{\theta_m}\right)^2} \quad (2)$$

$$\tau_r = \frac{\gamma_1}{\left|\varepsilon_0|\Delta\varepsilon|E^2 - \frac{4K_{33}}{L^2}\left(\frac{\pi}{2} - \frac{\theta_p}{\theta_m}\right)^2\right|} \quad (3)$$

where γ_1 is the LC rotational viscosity, L is the LC cell thickness, K_{33} represents the elastic constant, $\varepsilon_0\Delta\varepsilon E^2$ is the electric field energy density, $\Delta\varepsilon$ is the LC dielectric anisotropy, θ_p is the pretilt angle, and θ_m is the maximum tilt angle in the center of the LC cell. In addition to the character of the liquid itself, the temperature and the pretilt angle of the liquid crystal will have an influence on the response time. K_{33} and γ_1 decrease with an increase in temperature [27]. However, when the temperature changes, γ_1 has a greater influence than K_{33}. Therefore, the relaxation time decreases with increasing temperature. In addition, the pretilt angle of the LC will have an effect on the response time. In most cases, the maximum tilt angle is far larger than the pretilt angle. So, the response time will increase with the growth of the pretilt angle.

It is worth noting that the bias voltage (V) has effects on the LC response time, since θ_m decreases when the voltage becomes smaller. The pretilt angle effect becomes more pronounced when the voltage (V) gets close to the threshold voltage (V_{th}). In the $V_{th} < V < 4V_{th}$, θ_m increases significantly when the applied voltage increases and eventually approaches 90° [26]. When the voltage applied to the LC exceeds the V_{th}, the amount of delay begins to decrease as the voltage rises. Between the V_{th} and the $4V_{th}$, the phase delay falls faster, and above the $4V_{th}$, the phase delay changes slowly and closes to the minimum. The

bias voltage V affects the minimum delay acquired by the LC, because of the angle of LC molecules.

When light with a wavelength λ is normally incident on the surface of the LC cell, the phase difference $\Delta\varphi$ between the two polarized light beams can be expressed as $\Delta\varphi = 2\pi\Delta nL/\lambda$. The LC cell was located between two parallel polarizers, and the polarization axis was oriented at 45° with respect to the LC optical axis. The schematic in Figure 1a shows the delay between the dual beams emitted from the LC. Figure 1b illustrates the relationship between the molecular deformation of the LC and the dual-beam delay during the relaxation time. From left to right in the figure, the delay between the dual beams corresponds to the time when the LC returns from the high-energy state to the initial stable orientation distribution state. The dual-beam delay changes rapidly with the relaxation time of the LC.

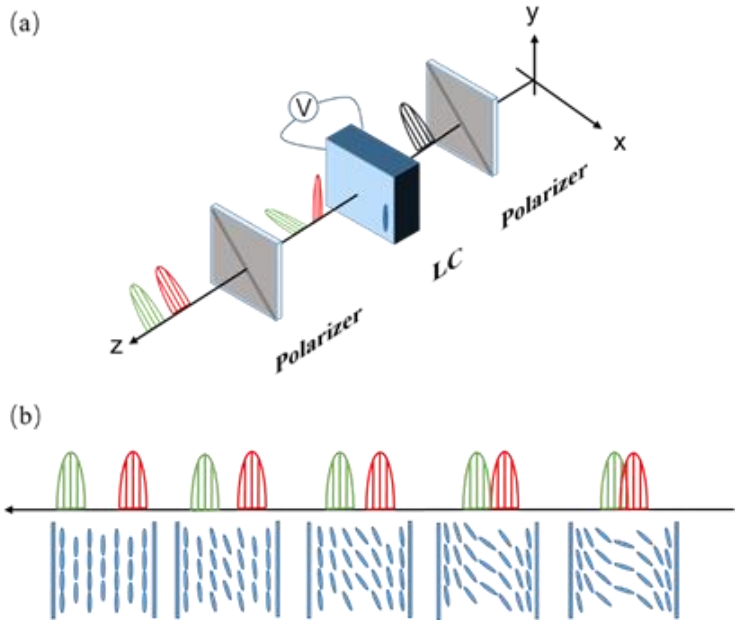


Figure 1. (**a**) Principle of measurement for the delay between the two beams provided by liquid crystal (LC). (**b**) Schematic of the relationship between the molecular deformation of the LC and the dual-beam delay during the relaxation time.

The relationship between the transmitted light intensity and the incident light intensity is given by Equation (4) [28]:

$$I = I_0\left(1 - \sin^2(\Delta\varphi/2)\right) \tag{4}$$

From the equation above, the light intensity reflects the phase change. Based on the above principles, the key to interferometric spectroscopy is to obtain the optical path difference and interference information at various instances in time. The relaxation time of thick LCs can be used to obtain a large optical path difference in a short time. Therefore, the variation in interference intensity with different optical path differences can be obtained in a short time by using the electro-controlled birefringence and relaxation properties of the LC.

3. Calibration of the Optical Path Difference at Different Times during the Relaxation of LC and Spectral Imaging Analysis

As shown in Figure 2, a LC cascade was placed between two parallel linear polarizers. The polarization direction of the two polarizers was 45° relative to the optical axis of the thick LC. A single-frequency distributed-feedback (DFB) fiber laser at 1053 nm, or a halogen light, was used to pass light through a collimating lens, which was selected by a flip-flop.

After the light was transmitted through the first polarizer, it changed to linearly polarized light. The light, with a polarization direction of 45° to the LC optical axis, was vertically incident on the surface of the LC cell. After the polarized light entered the LC, it split into two beams with an orthogonal polarization direction and equal amplitude component. After passing through the second polarizer, the two beams with a delay difference vibrated in the same direction. The delay difference changed with the rearrangement of the LC molecules. Finally, the spatial interferogram was obtained by a CCD high-speed camera with a detection frequency of 500 Hz.

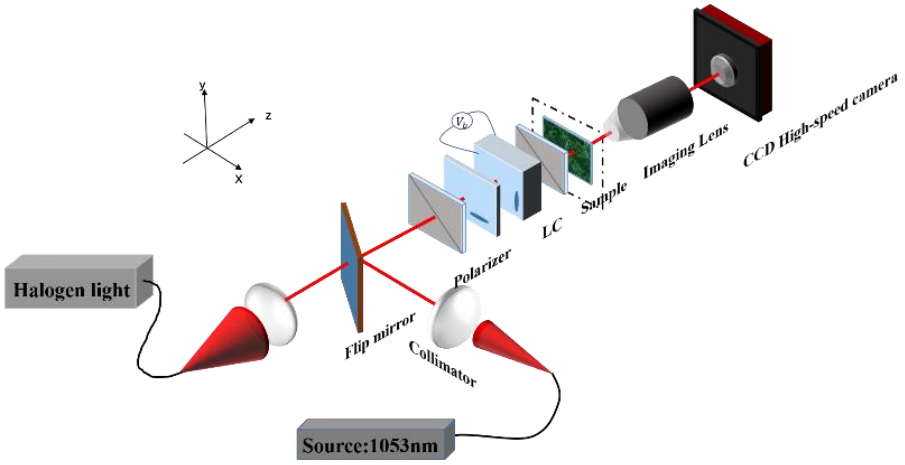


Figure 2. Experimental setup of the interference spectral imaging system based on LC relaxation.

From the phase difference expression $\Delta\varphi = 2\pi\Delta nL/\lambda$, the maximum optical path difference between the two beams is proportional to the LC thickness. The spectral resolution is inversely proportional to the introduced optical path difference. To enhance the spectral resolution, we need to consider the use of a thick LC. The thickness of the LC for dynamic driving in this study was 100 μm. It is worth noting that when using a thick LC cell only, the difference in the refraction index of the LC is not equal to 0 under the influence of the electric field owing to the strong anchoring effect. In order to acquire zero path difference, a thin LC with a thickness of 10 μm should be used as an optical path difference offset. The optical axis of the thin static LC is perpendicular to the optical axis of the thick LC [20]. Further, from the relationship between the phase difference and the thickness, it can be derived that the light needs to be incident, quasi-parallel, and perpendicular to the surface of the LC cell. Solutions to the above-mentioned limitations on the detection angle of the system are given in [15,29].

The thick LC cell was driven by a square electrical signal at 1 kHz. The LC relaxation was obtained by turning off the driving voltage V_m on the LC. The driving voltage will affect the optical path difference, since the maximum tilt angle decreases when the voltage becomes smaller. The optical path difference is essentially invariable about 5 v. In order to obtain the minimum delay difference, we used a 5 V driving voltage on the cell to obtain the complete optical path difference. During the LC relaxation, the interference intensity at different times was recorded using a high-speed CCD. The relationship between the optical path differences at different times during the relaxation period was calibrated by measuring the intensity of one pixel point at 1053 nm. Figure 3 shows the variation in interference intensity with LC relaxation time for 1053 nm and halogen light sources.

Using the data shown in Figure 3a, the intensity variation was converted into an optical path difference over time [30]. The obtained variation in delay with relaxation time is shown in Figure 4.

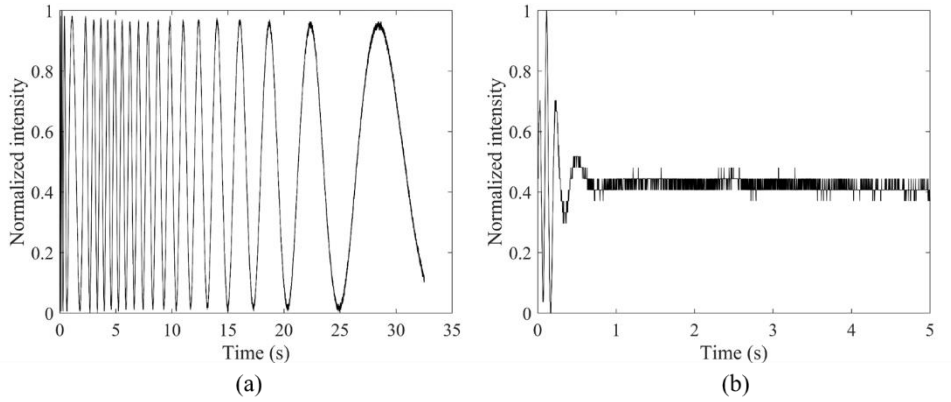


Figure 3. Interference light intensity variation with the relaxation time. t = 0 is the moment when the LC cell driving voltage $V_m = 5$ V is turned off. (**a**) The 1053 nm DFB fiber laser; (**b**) the halogen light.

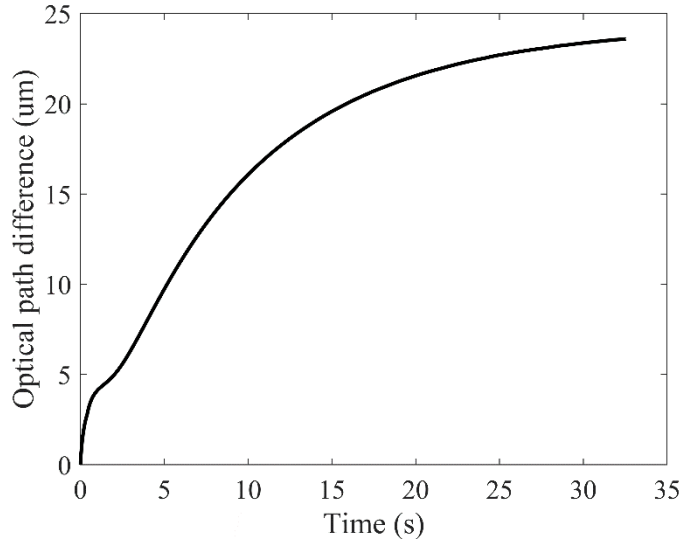


Figure 4. Relationship between the optical path difference delay and the LC relaxation time obtained at 1053 nm.

For the 100 μm LC cell, the impact of uniformity cannot be ignored. Nine measuring points at different LC positions are shown in Figure 5a. Figure 5b shows the optical path difference and error bars for each position limiting the vibration and temperature. From Figure 5b, the error is generally within 2% at different places during the same relaxation time. In addition, from the error bars at different places, it can be seen that the thickness of the right area of the LC is more uniform than that of the left area. Choosing a suitable beam size and position will reduce measurement errors. However, temperature changes are known to affect the birefringence and the response time of the LC. To reduce the impact of such errors, the system can be calibrated at different temperatures.

The premise of interconversion between interferogram data and spectrogram data is that the sampling interval must satisfy the sampling theorem, and samples must be at equal intervals. The optical path difference interval corresponding to the sampling interval of the interferogram in the experiment is $\Delta_e \leq 1/2\sigma_{max}$, where σ_{max} is the maximum wave number of the measured spectrum. Therefore, the calibration curve in Figure 4 was sampled with a constant optical path difference. Figure 6 shows the interferogram using the sampling theorem with 1053 nm laser light and wide-spectrum halogen light, respectively, with a constant step size. Figure 6a shows that the interferogram of the 1053 nm light is approximately equally spaced, which is typical of monochromatic light interference. Figure 6b shows typical broad-spectrum interference.

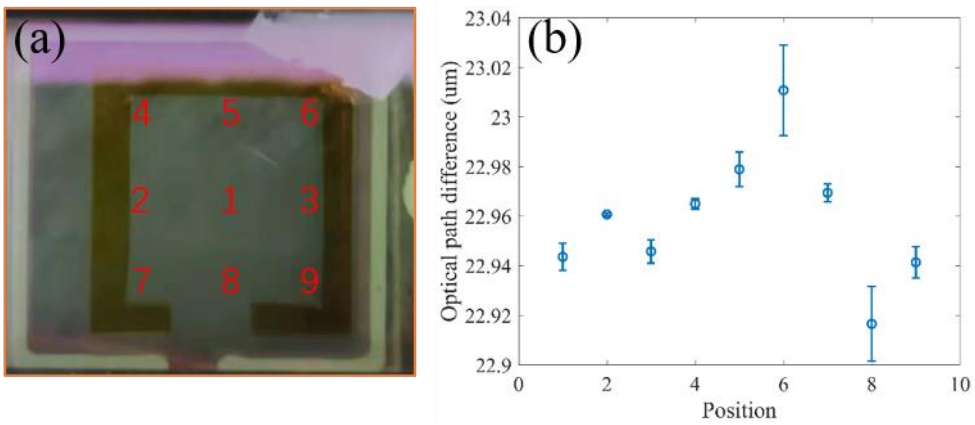


Figure 5. (**a**) Position of the measuring points for the LC. (**b**) Optical path difference and error bar at each position.

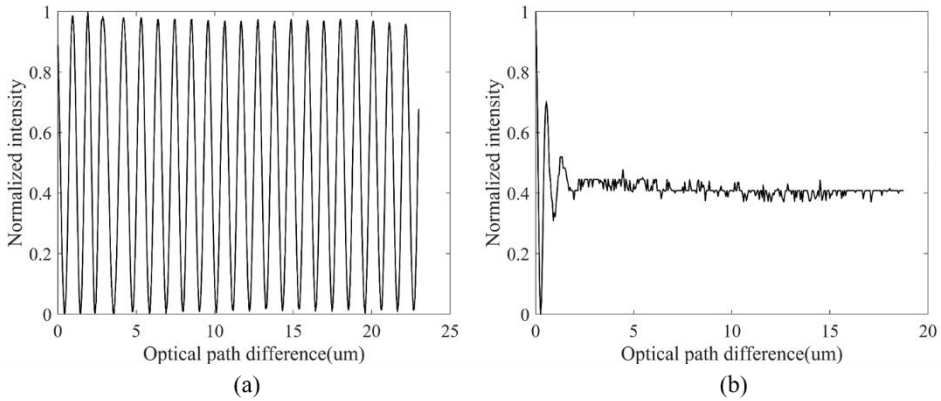


Figure 6. Variation in interference light intensity with optical path difference. (**a**) The 1053 nm light and (**b**) the wide-spectrum halogen light.

An effective interferogram was obtained after denoising, phase correction, and processing with an apodization function [22]. By applying the wavelet transform to the interferogram containing noise, an interferogram with reduced noise was obtained [31]. The wavelet transform has the advantages of Fourier analysis while being superior to it. Choosing a suitable number of decomposition layers and an adaptive threshold further enhances the denoising effect. Based on the principle of the single-side beyond-zero path difference, cascaded LC cells were used to obtain a single-sided asymmetric interferogram that passed through a 0 optical range difference, as shown in Figure 6b [32]. Using the interference maximum at 0 optical path difference, we obtained a double-sided symmetric interferogram. The interferogram in the experiment could only be collected at the position of the maximum optical range difference. Hence, to reduce the effect of side lobes caused by data truncation, the apodization function must be considered in the processing of the interferogram [33].

Using the effective interferogram, the recovered spectral information was obtained through the inverse Fourier transform, as shown in Figure 7.

In summary, the maximum optical path difference for 1053 nm light was $\Delta_{max} = 23$ µm. The full width at half-height (FWHH) of the instrumental line shape can be used to determine the limiting resolution of the recovery spectrum. The tangent function used in this study is a rectangular function, which corresponds to $\mathrm{FWHH} = 1.207/2\Delta_{max}$. The spectral resolution is calculated by $\mathrm{d}\lambda = \lambda^2 \times \mathrm{FWHH}$, where $\mathrm{d}\lambda$ is the spectral resolution at λ. The theoretical spectral resolution is 262 cm^{-1}, whereas the actual recovered spectral half-height width of 1053 nm light is 28.64 nm, as shown in Figure 6a. A thicker LC is required to obtain a larger optical path difference and further improve the spectral resolution.

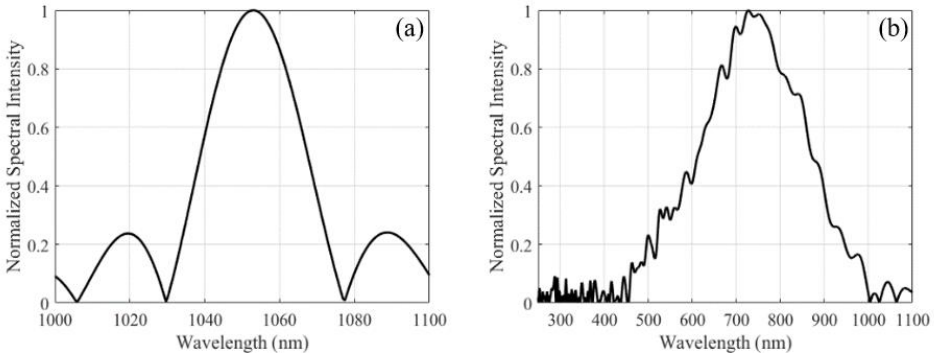


Figure 7. Recovery spectra of (**a**) 1053 nm and (**b**) halogen light.

4. Application of the Interferometric Spectral Image System Based on LC Delayers

Based on the calibration of the optical path difference at different times at a single pixel during the relaxation of the LC, hyperspectral imaging was performed using a resolution chart, where the sample was placed between the imaging lens and the second polarizer. The image was relayed to the high-speed camera. The signal generator was turned off so that the driving voltage (V_b) controlling the LC cell changed from 5 V to 0 V. A high-speed camera was used to acquire the spatial interferogram changes during the LC relaxation process over a 20-s period. The desired spectrum was obtained by Fourier processing of 400 images with useful two-dimensional spatial information selected from 10,000 images. By recovering the spectrum for each pixel point, a hyperspectral data cube was obtained and is shown in Figure 8, which characterizes the two-dimensional spatial information and one-dimensional spectral information.

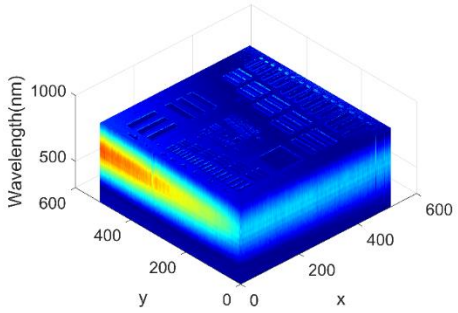


Figure 8. The hyperspectral data cube of the resolution chart.

Figure 9a shows the integrated two-dimensional spatial information acquired using the entire spectrum. Figure 9b–d show the two-dimensional spatial information at different wavelengths. Figure 9e–h, corresponding to Figure 9a–d, respectively, show the one-dimensional intensity information for x = 158 and y values from 200 to 280. Figure 9 shows that the spatial resolution is different for different wavelengths. The spatial resolution is 50.8 LP/mm when the wavelength is 650 nm, whereas the spatial resolution is 40.3 LP/mm when the entire spectrum is included. The spatial resolution of 650 nm is clearly higher than the values obtained for other spectral surfaces.

Considering the size of the damage point, K9 glass was utilized for the damage analysis of the sample. From Figure 10b, the spectra of the damaged and undamaged points can be obtained. Figure 10c,d indicate the one-dimensional intensity information acquired at x = 203 for the whole spectrum and at 580 nm. In Figure 10c, the minimum size of the damage point detected is 16 μm, while the minimum size of the damage point is 12 μm in Figure 10d. The information expressed in Figure 9 is further confirmed in Figure 10c,d. When white light was used as the source of illumination, light waves of different intensities and wavelengths were superimposed on each other, causing the defect information to be obscured or ignored. As shown in Figure 10, it can be observed that the

method of spectral imaging for defect detection can identify damage points that are not easily observed using a broadband source. So, choosing a suitable wavelength can improve the spatial resolution. It can be used in optical illumination for machine vision methods by effectively selecting the wavelength or combining multiple wavelengths of the light source. The proposed optical component defect inspection method based on interference spectral imaging on the basis of LC relaxation enables rapid non-destructive testing of optical components.

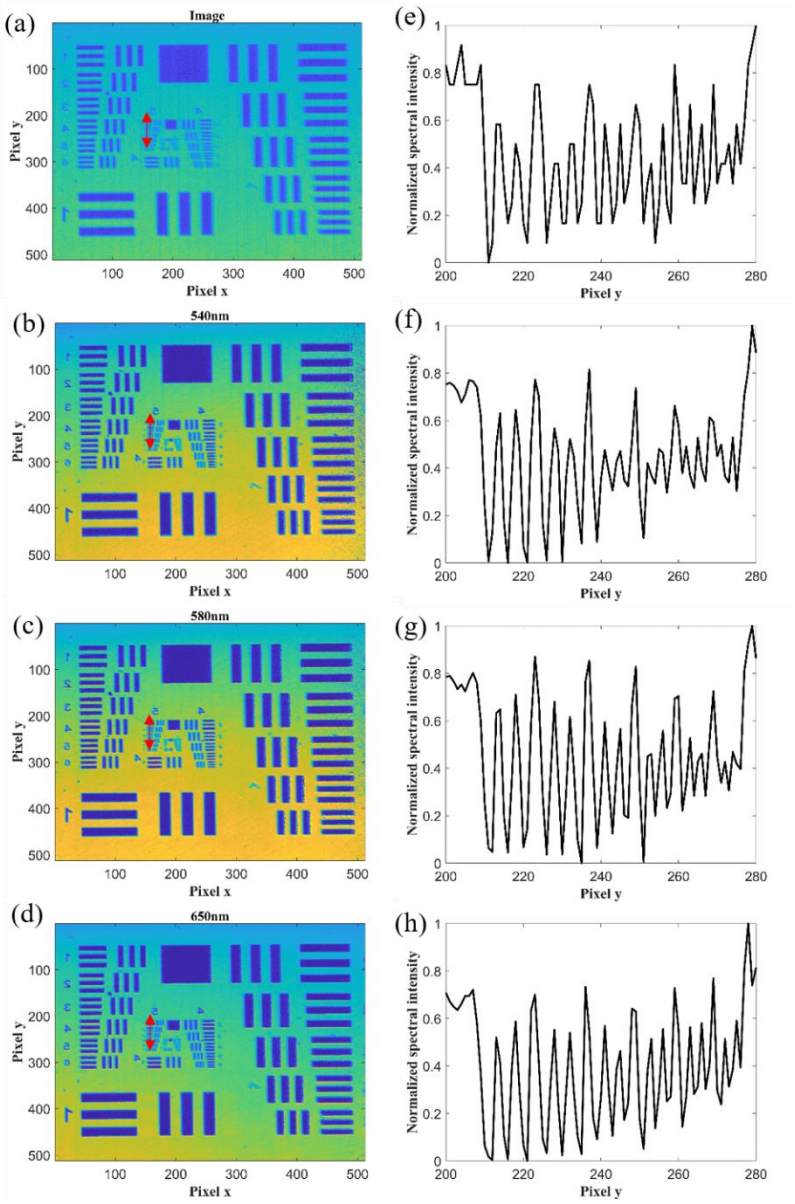


Figure 9. (**a**) Integration of the two-dimensional spatial information acquired for the whole spectrum. (**b**–**d**) The two-dimensional spatial information at 540 nm, 580 nm, and 650 nm. (**e**–**h**) correspond to (**a**–**d**) for the intensity information at each point for x = 158 and y values from 200 to 280.

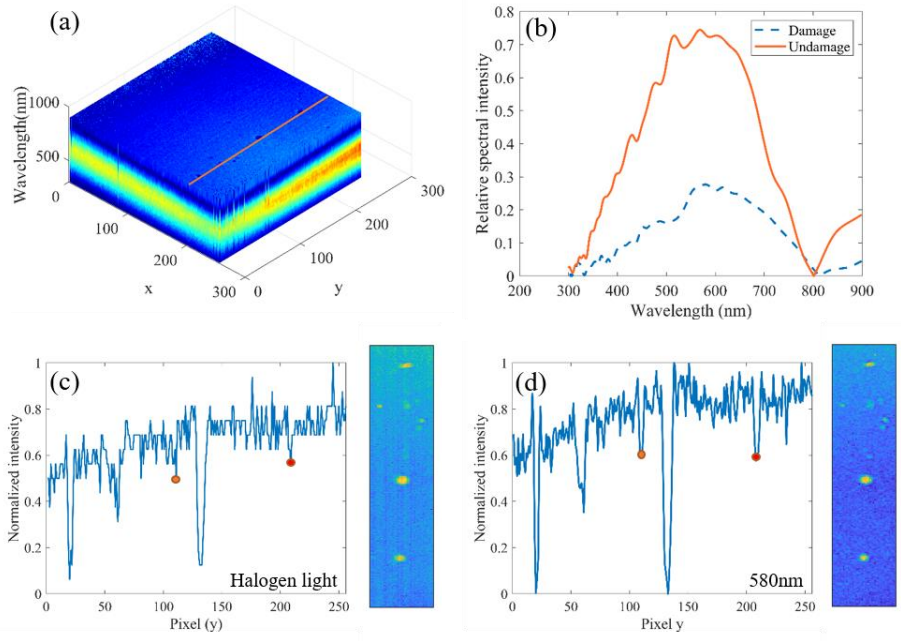


Figure 10. (**a**) Hyperspectral data cube of K9 glass. (**b**) The spectra of damaged and undamaged points. (**c**) From left to right, one-dimensional (x = 203) and two-dimensional (x = 200–240) spatial information for the entire spectrum. (**d**) From left to right, one-dimensional (x = 203) and two-dimensional (x = 200–240) spatial information at the indicated wavelengths (580 nm).

5. Conclusions

In conclusion, interference spectral imaging based on LC relaxation is proposed in this paper. A LC cascade composed of a thick LC (100 μm) and a thin LC (10 μm) provided an optical path difference of 23 μm. Calibration using monochromatic light (1053 nm) resulted in a spectral resolution of 262 cm^{-1} in the 400–1000 nm spectral range for the system. Spatial interference data could be obtained quickly in a measurement period of 20 s. This method was also used to measure the transmission spectra of resolution plates and optical damage to elements, which verified its feasibility in hyperspectral imaging and optical component damage detection.

The performance of the system could be further improved by considering the relationship between the refractive index of the LC and the wavelength in the calibration and by increasing the field of view angle. The spectral responsivity of individual components should be considered in the spectral line calibration procedure. Finally, the proposed interferometric spectroscopy imaging technique has several advantages, such as rapid performance, a low cost, high stability, and easy integration. It could be further used for performance improvements in applications such as spectral microscopy and portable spectrometry.

Author Contributions: Conceptualization, J.Y. and W.F.; methodology, J.Y. and D.H.; software, J.Y and T.D.; validation, J.Y.; formal analysis, D.H.; investigation, H.C. and T.D.; resources, W.F. and H.C.; data curation, J.Y. and W.F.; writing—original draft preparation, J.Y. and W.F.; writing—review and editing, W.F. and J.Y.; visualization, W.F.; supervision, W.F.; project administration, W.F.; funding acquisition, W.F. All authors have read and agreed to the published version of the manuscript.

Funding: This work was supported by the Strategic Priority Research Program of the Chinese Academy of Sciences (No. XDA25020303).

Institutional Review Board Statement: Not applicable.

Informed Consent Statement: Not applicable.

Data Availability Statement: The data included in this study are all owned by the research group and will not be made available.

Acknowledgments: We acknowledge the financial support of Self Deployed Projects of Shanghai Institute of Optics and Fine Mechanics, Chinese Academy of Sciences.

Conflicts of Interest: The authors declare no conflict of interest.

References

1. Ren, Z.; Fang, F.; Yan, N.; Wu, Y. State of the Art in Defect Detection Based on Machine Vision. *Int. J. Precis. Eng. Manuf.-Green Technol.* **2021**, 1–31. [CrossRef]
2. Hristu, R.; Stanciu, S.G.; Tranca, D.E.; Matei, A.A.; Stanciu, G. Nonlinear optical imaging of defects in cubic silicon carbide epilayers. *Sci. Rep.* **2014**, *4*, 5258. [CrossRef]
3. Torres, J.A.; Torres-Torres, C.; Vidal, E.; Fernández, F.; de Icaza-Herrera, M.; Loske, A.M. Violin vibration state determined from laser streak patterns. *Appl. Acoust.* **2021**, *185*, 108384. [CrossRef]
4. Hsieh, C.-F.; Yang, C.-S.; Shih, F.-C.; Pan, R.-P.; Pan, C.-L. Liquid-crystal-based magnetically tunable terahertz achromatic quarter-wave plate. *Opt. Express* **2019**, *27*, 9933–9940. [CrossRef]
5. Melnyk, O.; Jones, R.; Macêdo, R.; Garbovskiy, Y.; Hagen, G.; Glushchenko, A.V.; Spendier, K.; Camley, R.E. Fast Switching Dual-Frequency Nematic Liquid Crystal Tunable Filters. *ACS Photon.* **2021**, *8*, 1222–1231. [CrossRef]
6. Yang, Y.; Liu, X.; Wu, Y.; Li, T.; Fan, F.; Huang, H.; Wen, S. Optical edge detection with adjustable resolution based on liquid crystal polarization gratings. *Chin. Opt. Lett.* **2020**, *18*, 093501. [CrossRef]
7. Qi, X.; Fan, W.; Huang, D.; Xia, G.; Cheng, H.; Shi, Z.-D. Analysis of factors affecting delay accuracy of subfemtosecond liquid crystal variable retarders. *Appl. Opt.* **2020**, *59*, 6984. [CrossRef]
8. Zhang, H.; Shang, J.; Liu, X.; Sun, W.; Wang, F.; Liu, Y. High-sensitivity fiber liquid crystals temperature sensor with tiny size and simple tapered structure. *Chin. Opt. Lett.* **2020**, *18*, 101202. [CrossRef]
9. Gao, S.; Wang, J.; Li, W.; Yu, X.; Zhang, X.; Song, X.; Iljin, A.; Drevensek-Olenik, I.; Rupp, R.A.; Xu, J. Low threshold random lasing in dye-doped and strongly disordered chiral liquid crystals. *Photon. Res.* **2020**, *8*, 642. [CrossRef]
10. Shen, Z.; Zhou, S.; Li, X.; Ge, S.; Chen, P.; Hu, W.; Lu, Y. Liquid crystal integrated metalens with tunable chromatic aberration. *Adv. Photon.* **2020**, *2*, 036002. [CrossRef]
11. Blouke, M.M.; Shingu, H.; Homma, K.; Kurosaki, H.; Suzuki, T.; Yamamoto, H.; Canosa, J.; Sampat, N. Development of an onboard spectro-polarimeter for Earth observation at NAL. In Proceedings of the Sensors and Camera Systems for Scientific, Industrial, and Digital Photography Applications III, San Jose, CA, USA, 21–23 January 2002; Sampat, N., Canosa, J., Eds.; SPIE: Bellingham, WA, USA, 2002; pp. 89–97. [CrossRef]
12. Abuleil, M.; Abdulhalim, I. Narrowband multispectral liquid crystal tunable filter. *Opt. Lett.* **2016**, *41*, 1957–1960. [CrossRef]
13. Shi, W.; Zhou, P.; Liu, Z.; Wang, L.; Jiang, S.; Mi, Z.; Yan, K.; Zhang, T.; Zhao, H.; Guo, Q.; et al. Narrow bandwidth liquid crystal tunable filter based on Lyot-Solc composite structure. In Proceedings of the Advanced Laser Technology and Applications, Beijing, China, 22–24 May 2018; Jiang, S., Wang, L., Eds.; SPIE: Bellingham, WA, USA, 2018.
14. Wang, X.; Zhang, Y.; Ma, X.; Xu, T.; Arce, G.R. Compressive spectral imaging system based on liquid crystal tunable filter. *Opt. Express* **2018**, *26*, 25226–25243. [CrossRef]
15. Itoh, K.; Inoue, T.; Ohta, T.; Ichioka, Y. Liquid-crystal imaging Fourier-spectrometer array. *Opt. Lett.* **1990**, *15*, 652–654. [CrossRef] [PubMed]
16. LaMarr, B.J.; Bautz, M.W.; Foster, R.; Grant, C.E.; Malonis, A.; Miller, E.D.; Prigozhin, G.; Thayer, C.; den Herder, J.-W.A.; Nakazawa, K.; et al. Radiation testing of a small pixel, CMOS compatible CCD. In Proceedings of the Space Telescopes and Instrumentation 2020: Ultraviolet to Gamma Ray, Online, 14–18 December 2020; Herder, J., Nikzad, S., Eds.; SPIE: Bellingham, WA, USA, 2020.
17. Hegyi, A.; Martini, J. Hyperspectral imaging with a liquid crystal polarization interferometer. *Opt. Express* **2015**, *23*, 28742–28754. [CrossRef] [PubMed]
18. Xia, L.; Yang, Z.; Yin, S.; Deng, Q.; Du, C. Method of realizing compact Fourier transform spectrometer without moving parts based on birefringent liquid crystal. *Opt. Eng.* **2014**, *53*, 74109. [CrossRef]
19. Jullien, A.; Pascal, R.; Bortolozzo, U.; Forget, N.; Residori, S. High-resolution hyperspectral imaging with cascaded liquid crystal cells. *Optica* **2017**, *4*, 400–405. [CrossRef]
20. Jullien, A.; Scarangella, A.; Bortolozzo, U.; Residori, S.; Mitov, M. Nanoscale hyperspectral imaging of tilted cholesteric liquid crystal structures. *Soft Matter* **2019**, *15*, 3256–3263. [CrossRef]
21. Shmilovich, S.; Oiknine, Y.; Abuleil, M.; Abdulhalim, I.; Blumberg, D.G.; Stern, A. Dual-camera design for hyperspectral and panchromatic imaging, using a wedge shaped liquid crystal as a spectral multiplexer. *Sci. Rep.* **2020**, *10*, 3455. [CrossRef]
22. Oriana, A.; Réhault, J.; Preda, F.; Polli, D.; Cerullo, G. Scanning Fourier transform spectrometer in the visible range based on birefringent wedges. *J. Opt. Soc. Am. A* **2016**, *33*, 1415. [CrossRef]
23. Di Pietro, V.M.; Jullien, A.; Bortolozzo, U.; Forget, N.; Residori, S. Dynamical optical response of nematic liquid crystal cells through electrically driven Fréedericksz transition: Influence of the nematic layer thickness. *Opt. Express* **2018**, *26*, 10716–10728. [CrossRef]
24. Yang, D.K.; Wu, S.T. Transmissive Liquid Crystal Displays. In *Fundamentals of Liquid Crystal Devices*, 2nd ed.; Yang, D.K., Wu, S.T., Eds.; E-Publishing Inc.: New York, NY, USA, 2014; pp. 235–283.

25. Huang, Z.Q. Relaxation characteristics of liquid crystal. In *Principle of Liquid Crystal Display*; National Defense Industry Press: Beijing, China, 2006; pp. 184–192.
26. Nie, X.; Xianyu, H.; Lu, R.; Wu, T.X.; Wu, S.-T. Pretilt Angle Effects on Liquid Crystal Response Time. *J. Disp. Technol.* **2007**, *3*, 280–283. [CrossRef]
27. Huang, Y.-X.; Tu, M. Dependence of viscoelastic parameters of nematic liquid crystals on pretilt angle and temperature. *Curr. Appl. Phys.* **2010**, *10*, 561–564. [CrossRef]
28. Wu, S.-T.; Efron, U.; Hess, L.D. Birefringence measurements of liquid crystals. *Appl. Opt.* **1984**, *23*, 3911–3915. [CrossRef]
29. Lee, Y.-H.; Franklin, D.; Gou, F.; Liu, G.-G.; Peng, F.; Chanda, D.; Wu, S.-T. Two-photon polymerization enabled multi-layer liquid crystal phase modulator. *Sci. Rep.* **2017**, *7*, 16260. [CrossRef]
30. Lopez-Tellez, J.M.; Bruce, N.C.; Delgado-Aguillón, J.; Garduño-Mejía, J.; Avendaño-Alejo, M. Experimental method to characterize the retardance function of optical variable retarders. *Am. J. Phys.* **2015**, *83*, 143–149. [CrossRef]
31. Bachman, G.; Narici, L.; Beckenstein, E. Wavelets. In *Fourier and Wavelet Analysis*; Springer: New York, NY, USA, 2000; pp. 411–487.
32. Ben-David, A.; Ifarraguerri, A. Computation of a spectrum from a single-beam fourier-transform infrared interferogram. *Appl. Opt.* **2002**, *41*, 1181–1189. [CrossRef]
33. Harris, F.J. On the use of windows for harmonic analysis with the discrete Fourier transform. *Proc. IEEE* **2005**, *66*, 51–83. [CrossRef]